

Modeling differential rotations of compact stars in equilibriums

Kōji Uryū,¹ Antonios Tsokaros,² Luca Baiotti,³ Filippo Galeazzi,⁴ Keisuke Taniguchi,¹ and Shin'ichirou Yoshida⁵

¹*Department of Physics, University of the Ryukyus, Senbaru, Nishihara, Okinawa 903-0213, Japan*

²*Department of Physics, University of Illinois at Urbana-Champaign, Urbana, IL 61801*

³*Graduate School of Science, Osaka University, 560-0043 Toyonaka, Japan*

⁴*Kurfürstenallee 24C, 28211 Bremen, Germany*

⁵*Department of Earth Science and Astronomy, Graduate School of Arts and Sciences,*

The University of Tokyo, Komaba, Tokyo 153-8902, Japan

(Dated: March 13, 2022)

Outcomes of numerical relativity simulations of massive core collapses or binary neutron star mergers with moderate masses suggest formations of rapidly and differentially rotating neutron stars. Subsequent fall back accretion may also amplify the degree of differential rotation. We propose new formulations for modeling the differential rotation of those compact stars, and present selected solutions of differentially rotating, stationary, and axisymmetric compact stars in equilibrium. For the cases when rotating stars reach break-up velocities, the maximum masses of such rotating models are obtained.

I. INTRODUCTION

According to numerical relativity simulations, compact stars have a significant amount of differential rotation in two cases. One is proto neutron stars (PNS) formed after the core collapses of supernova progenitors around $8 - 25M_{\odot}$, and the other is hypermassive neutron stars (HMNS) formed after binary neutron star (BNS) mergers [1, 2]. The rotation curve of PNS, roughly speaking the angular velocity profile Ω as a function of the cylindrical radial coordinate $\varpi = r \sin \theta$, may depend on various factors including initial spins, magnetic field configurations, and equations of state (EOS), and may evolve in time with a timescale longer than the dynamical one.

It has been reported in recent core collapse simulations that in the range $\sim 20 - 30\text{km}$ from the rotation axis the rotation curves are monotonically decreasing of about a few tens of % from the value at the rotation axis [3]. The rotation curves of the HMNS formed after binary neutron star mergers are more complex. Recent simulations [4] suggest that the profile of the rotation curve $\Omega(\varpi)$ increases of about a few tens to a few hundreds of % of the central value Ω_c and then decreases, independently of EOS. Not only the above dynamical process, but also the subsequent fall back accretion may amplify the degree of differential rotations [5]. If the matter from a fall back disk accretes onto the equatorial surface of a nascent neutron star to spin it up, the angular velocity of the outer part of neutron star could become even faster than the inner part.

Modeling such differential rotations in the relativistic regime is important for accurately computing stationary and axisymmetric equilibriums of the above mentioned astrophysical compact objects. Such equilibrium solutions will be useful for studying their long time evolutions in thermal/viscous timescales, for studying their dynamical or secular stabilities, and for providing initial data for numerical relativity simulations [6]. Stationary and axisymmetric models of rapidly rotating stars can be calculated most straightforwardly by deriving an an-

alytic first integral of the Euler equation, and by simultaneously solving the first integral and the gravitational field potentials using a certain iterative, self-consistent, numerical method [7, 8]. In Newtonian gravity, the first integral can be derived assuming a one-parameter EOS for the thermodynamic variables (namely, a barotropic fluid), or the flow field to be $v^a = \Omega \phi^a$, where the angular velocity Ω depends only on ϖ , $\Omega = \Omega(\varpi)$. Either one of these choices implies the other condition [9].¹

In the case of relativistic gravity, the relativistic Euler equation associated with the timelike and rotational Killing fields t^α and ϕ^α can be analytically integrated for the circular flow, $u^\alpha = u^t(t^\alpha + \Omega \phi^\alpha)$, where u^α is the 4 velocity of the perfect fluid. Different from the Newtonian case, however, the integrability condition can not be expressed as Ω to be a function of coordinate ϖ , but as the relativistic specific angular momentum $j := u^t u_\phi$ ($u_\phi := u_\alpha \phi^\alpha$) to be a function of Ω , $j = j(\Omega)$ [6]. For this condition, it is less clear than the Newtonian case how one should set the form of the integrability condition $j(\Omega)$. Because of this, only limited types of differential rotations have been investigated for relativistic stars [10–13].

The differential rotation law used in most of previous works is the so called j -constant law

$$j(\Omega) = A^2(\Omega_c - \Omega), \quad (1)$$

where Ω_c and A are constants. One of the well known applications of this rotation law is the computation of HMNS formed after binary neutron star mergers. Baumgarte, Shapiro, and Shibata (BSS) [11] have shown that this rotation law can support stars having nearly twice of the maximum mass of the non-rotating star for the same EOS. This work was extended by several authors using

¹ In this paper, the Latin indices denote spatial vectors or tensors, the Greek indices spacetime ones, and geometric units $G = c = 1$ with solar mass $M_{\odot} = 1$ are used.

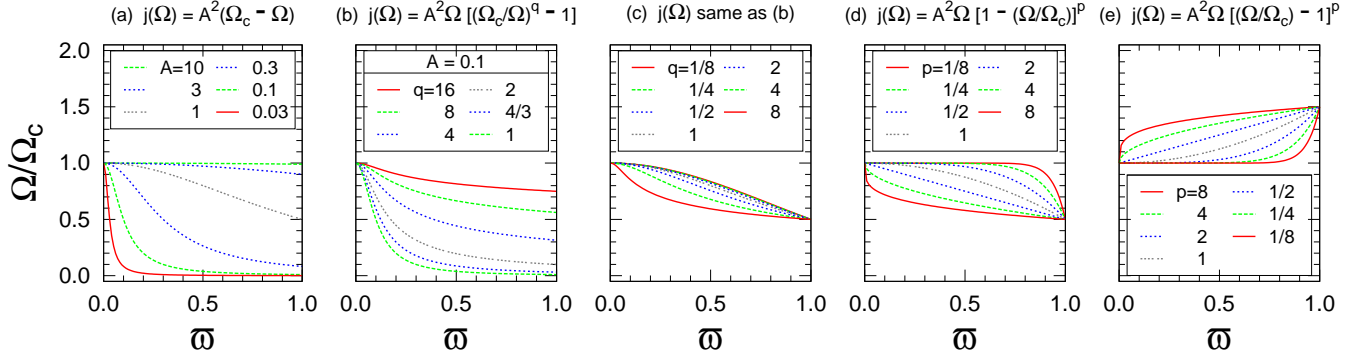


FIG. 1. Rotation curves $\Omega(\varpi)$ for the rotation laws (1), (4) and (5) in the Newtonian limit. Panel(a): j -constant law (1) (whose $\Omega(\varpi)$ is the left expression in Eq.(6) with $q = 1$). Panel(b): Eq. (4) with $A = 0.1$ ($\Omega(\varpi)$ is the left expression in Eq. (6)). Panel(c): same as panel(b), Eq. (4) but with $\Omega_{\text{eq}}/\Omega_c = 0.5$. Panel(d): a new rotation law (5) with a negative sign ($\Omega(\varpi)$ is the right expression in Eq. (6) with a negative sign). Panel(e): a new rotation law (5) with a positive sign ($\Omega(\varpi)$ is the right expression in Eq. (6) with a positive sign). For the cases of panel(c)-(e), the parameter A is determined by setting $\Omega_{\text{eq}}/\Omega_c = 0.5$, where Ω_c and Ω_{eq} are the angular velocities at the rotation axis and at the equatorial surface, respectively. In each panel, the order of the labels in the legends (from top left to bottom right) correspond the order of the curves in the plot (from top to bottom).

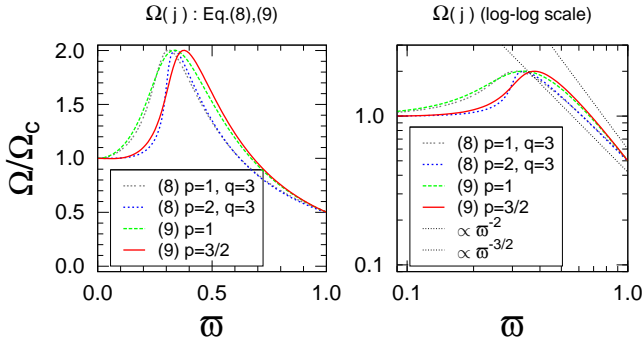


FIG. 2. Selected rotation curves $\Omega(\varpi)$ for the rotation laws (8) and (9) in the Newtonian limit. Left and right panels are the same curves in linear and log-log scales, respectively. The parameters A and B are determined by setting $\Omega_{\text{eq}}/\Omega_c = 0.5$ and $\Omega_{\text{max}}/\Omega_c = 2$, where Ω_{max} is the maximum angular velocity at a given point on the equatorial plane.

the same rotation law [12, 13]. However, this rotation curve (approximately, the curve labeled $A = 1$ in panel (a) of Fig.1) is even qualitatively different from the ones resulting from the simulations mentioned above [4]. To our knowledge, differential rotation laws different from Eq. (1) have been used only in [14–16] for computing compact stars, and in [17] for a rotating self-gravitating disk around a point source in first order post-Newtonian gravity.

In this paper, we introduce new formulations for modeling realistic rotation curves of differentially rotating compact stars extending our previous works [14, 16] and present the first results of the set of equilibrium solutions.

II. NEW FORMULATIONS FOR THE RELATIVISTIC DIFFERENTIAL ROTATIONS

The relativistic Euler equations are derived from the transverse components of the conservation laws, $\nabla_\beta T^{\alpha\beta} = 0$, with respect to the 4 velocity u^α , where the perfect fluid stress energy tensor is written $T^{\alpha\beta} = (\epsilon + p)u^\alpha u^\beta + pg^{\alpha\beta}$. Here, ϵ is the energy density, p the pressure, and $g^{\alpha\beta}$ the spacetime metric. Applying the symmetries along the timelike and rotational Killing fields t^α and ϕ^α , they are written

$$\nabla_\alpha \ln \frac{h}{u^t} + u^t u_\phi \nabla_\alpha \Omega - \frac{T}{h} \nabla_\alpha s = 0, \quad (2)$$

where h is the relativistic enthalpy defined by $h = (\epsilon + p)/\rho$, ρ the baryon rest mass density, T the temperature, and s the specific entropy. In this article, we assume a homentropic fluid $s = \text{constant}$, although an extension to a more general barotropic fluid is straightforward. Then, with the integrability condition $j := u^t u_\phi = j(\Omega)$, Eq. (2) is analytically integrated as

$$\frac{h}{u^t} \exp \left[\int j d\Omega \right] = \mathcal{E}, \quad (3)$$

where \mathcal{E} is a constant.

The choice of the function form of the integrability condition $j(\Omega)$ is the key for modeling various rotation curves in relativistic stars. In our previous paper [16], the following rotation law has been introduced

$$j(\Omega; q, A) = A^2 \Omega \left[\left(\frac{\Omega_c}{\Omega} \right)^q - 1 \right]. \quad (4)$$

² The relativistic enthalpy h satisfies the local thermodynamic relation $dh = Tds + dp/\rho$.

In addition to this, we propose new rotation laws,

$$j(\Omega; p, A) = A^2 \Omega \left[\mp \left(\frac{\Omega}{\Omega_c} - 1 \right) \right]^p. \quad (5)$$

The rotation laws (4) and (5) can be combined in a general form $j(\Omega; p, q, A) = A^2 \Omega [\mp ((\Omega_c/\Omega)^q - 1)]^p$. However, we separate them as (4) and (5), because they are general enough, and because the integrals of $j(\Omega; p, q, A)$ that appear in Eq. (3) involve hypergeometric functions for arbitrary values of the indices (p, q) , which may be inconvenient for a numerical code. The minus and plus signs of the rotation law (5) give monotonically decreasing and increasing rotation curves, respectively, by choosing a set of positive real roots for Ω which satisfies $\mp \left(\frac{\Omega}{\Omega_c} - 1 \right) > 0$ (see below). We usually choose the power indices p and q in Eqs. (4) and (5) to be positive real numbers.

In the Newtonian limit, $\Omega(\varpi)$ can be solved from $u^t u_\phi = \varpi^2 \Omega = j(\Omega)$ for each rotation law (4) and (5), respectively, as

$$\frac{\Omega}{\Omega_c} = \left(1 + \frac{\varpi^2}{A^2} \right)^{-1/q}, \quad \text{and} \quad \frac{\Omega}{\Omega_c} = 1 \mp \left(\frac{\varpi^2}{A^2} \right)^{1/p}. \quad (6)$$

From Eqs. (6), it becomes clear that the role of the parameter A , which has the dimension of length, is to set the radius where the rotation curve changes from a constant Ω_c to a certain differential rotation at a radius around $\varpi \sim A$. As discussed in [16], for the case of rotation law (4), which corresponds to the first rotation curve in Eq. (6), Ω becomes a power of ϖ , namely $\Omega \sim \varpi^{-2/q}$, in the Newtonian limit for $A \lesssim \varpi \leq R_0$, where R_0 is the equatorial radius of the compact star. For example, it becomes the Kepler rotation law for $q = 4/3$ and the j -constant law for $q = 1$, as shown in panel (b) of Fig. 1. In the regime of strong gravity, rotation profiles are modified because of relativistic effects (including the choice of coordinate conditions). Some examples are shown for selected solutions in the later section.

This rotation law (4) may be used in a different manner: by adjusting the constant parameter A for a given slope index parameter q , one can fix the value of Ω at a given point to a given value. For example, we can fix the ratio of Ω at the equatorial surface Ω_{eq} to its central value Ω_c , and vary the slope of the rotation curve $\Omega(\varpi)$. In panel (c) of Fig.1, such rotation curves $\Omega(\varpi)$ of Eq. (4) in the Newtonian limit (the first equation in (6)) are plotted for $\Omega_{\text{eq}}/\Omega_c = 0.5$. When the positive index q is decreased, one might expect that the rotation curves become more and more convex upward. However, as seen in panel (c), it is not the case: the slopes of the rotation curves with fixed $\Omega_{\text{eq}}/\Omega_c$ do not change very much for $0 < q < 1$.

This is one of the motivations for introducing new rotation laws (5) whose Newtonian limits are the expressions on the right in equation (6). For the case with the minus sign in Eq. (5), the slope of the rotation curves changes

gradually from convex downward to upward as the value of the positive index p decreases. This is shown in panel (d) of Fig. 1 for the Newtonian limit. For the case with the plus sign in Eq. (5), the rotation curves monotonically increase along the equatorial radius, and their Newtonian limit is plotted in the panel (e) of Fig. 1. As mentioned in the Introduction, these rotation laws with minus and plus signs may be used for modeling the evolution of the angular momentum distribution of the core of PNS and HMNS, or of neutron stars spinning up because of fall back accretion.

For the case of HMNS formed after BNS mergers, results of the simulations suggest that $j(\Omega)$ could become a multi-valued function. Therefore, we propose the integrability condition to be Ω as a function of j , $\Omega = \Omega(j)$, instead of $j = j(\Omega)$.³ Accordingly the integral in Eq. (3) should be rewritten,

$$\int j d\Omega = \int j \frac{d\Omega}{dj} dj. \quad (7)$$

Then, we propose two rotation laws,

$$\Omega(j; p, q, A, B) = \Omega_c \frac{1 + (j/B^2 \Omega_c)^p}{1 + (j/A^2 \Omega_c)^{q+p}}. \quad (8)$$

$$\Omega(j; p, A, B) = \Omega_c \left[1 + \left(\frac{j}{B^2 \Omega_c} \right)^p \right] \left(1 - \frac{j}{A^2 \Omega_c} \right). \quad (9)$$

In Fig.2, rotation curves in the Newtonian limit are plotted for selected indices $(p, q) = (1, 3)$ and $(2, 3)$ for Eq. (8), and $p = 1$ and 1.5 for Eq. (9). In these curves, we determine the parameters A and B by setting the ratio of the maximum value of Ω , Ω_{max} to that at the rotation axis Ω_c , as well as the ratio Ω_{eq} to Ω_c to be a given constant. In Fig.2, these ratios are set as $\Omega_{\text{max}}/\Omega_c = 2$ and $\Omega_{\text{eq}}/\Omega_c = 0.5$.

In both (8) and (9), the index p controls the growth of rotation curves near the rotation axis. This is analogous to the rotation law (5) with the positive sign, but for (8) and (9), $\Omega \sim \varpi^{2p} + \text{constant}$. The index q in Eq. (8) controls the asymptotic behavior of $\Omega(\varpi)$, in particular the index value $q = 3$ results in the Kepler rotation law in the Newtonian limit. For non integer values of (p, q) , the hypergeometric function appears in the first integral. Therefore, in actual applications of the rotation law (8), we choose indices $(p, q) = (1, 3)$ and $(2, 3)$ only. With these choices, the integral (7) becomes a little lengthy but analytic expressions in terms of elementary functions exist.

³ Eq. (2) is also written $\frac{\nabla_\alpha p}{\epsilon+p} - \nabla_\alpha \ln u^t + j \nabla_\alpha \Omega = 0$, and the relativistic von Zeipel's theorem states that the coincidence of the surfaces of constant energy density ϵ and pressure p is guaranteed if and only if $f(j, \Omega) = 0$, where f is a function of Ω and $j = u^t u_\phi$ only (or $f(l, \Omega) = 0$ where $l := -\frac{u_\phi}{u_t} = \frac{j}{1+j\Omega}$) [18].

TABLE I. The maximum mass and compactness of a spherically symmetric (Tolman-Oppenheimer-Volkov) solution for the case of the polytropic EOS $p = K\rho^\Gamma$ with $\Gamma = 2$. M_0 is the rest mass, M the gravitational mass, and M/R the compactness (R the circumferential radius). The constant K is chosen so that $M_0 = 1.5$ at $M/R = 0.2$. To convert the value of ρ_c in cgs units to that in $G = c = M_\odot = 1$ units, divide the value by $M_\odot (GM_\odot/c^2)^{-3} \approx 6.176393 \times 10^{17} \text{ g cm}^{-3}$.

Γ	$(p/\rho)_c$	ρ_c [g/cm ³]	M_0	M	M/R
2	0.318244	2.76957×10^{15}	1.51524	1.37931	0.214440

TABLE II. Parameters of the rotation laws used for computing equilibrium solutions presented in Fig.3. Models I to V and DR correspond to the pair of panels in Fig.3 in order from top to bottom in the left column, then top to bottom in the right column. Model DR is one of the HMNS solutions calculated in BSS [11].

Model	Rotation law	p	q	A/R_0	$\Omega_{\text{eq}}/\Omega_c$	$\Omega_{\text{max}}/\Omega_c$
I	(5) (minus)	1/4	—	—	0.5	—
II	(5) (plus)	1/2	—	—	0.5	—
III	(4)	—	4	$10^{-3/2}$	—	—
IV	(8)	1	3	—	0.5	2
V	(9)	3/2	—	—	0.5	2
DR	(4)	—	1	1	—	—

Rotation laws of the envelope or disk of matter ejected during events of core collapses or BNS mergers seem more likely to follow asymptotically the j -constant law as the remnants evolve toward axisymmetric configurations. Model (8), however, can not reproduce j -constant rotation in a region $A \lesssim \varpi \leq R_0$. Such a j -constant law in the envelope can be achieved by rotation law (9). For Eq. (9), one can integrate Eq.(7) analytically for any arbitrary values of p in terms of elementary functions. When the constant B is set to be $B > A$ in order to have $\Omega_{\text{max}} \sim \Omega_c$, this rotation law results in the j -constant law as in Eq.(1). However, for Eq.(9), Ω transits from uniform rotation to the j -constant rotation law more sharply than Eq.(1).

These rotation laws (1), (4), (5), (8), (9) are incorporated successfully into our COCAL code [16, 19]. In the following calculations, we use the Isenberg Wilson Mathews formulation (thin sandwich formalism), which is based on the 3+1 decomposition of the spacetime with the assumption of conformally flat spatial metric on the spacelike hypersurface. We also assume that the high density matter of compact stars is a perfect fluid whose EOS is approximated by a polytropic EOS $p = K\rho^\Gamma$ with the index $\Gamma = 2$ (see Table I). Further details on the formulation and numerical method can be found in our previous papers [16, 19].

III. RESULTS

In Fig.3, solutions of representative models for compact stars with various differential rotation laws are presented. In the left panel of each pair in the figure, shown are the contours for the rest mass density ρ , the color map for the distribution of the angular velocity Ω (normalized to the equatorial radius R_0), and the deformation sequence of the stellar surfaces (dashed green curves) in the xz (meridional) plane⁴. In the right panels, the rest mass density profile ρ/ρ_c and the rotation curve Ω/Ω_c normalized to the central value of each quantity are plotted along the radial coordinate ϖ in the equatorial plane.

Selected parameters for the differential rotation laws corresponding to the models in Fig.3 are summarized in TableII. Physical quantities of these selected solutions are listed in Table III. Also listed are, for reference, the differentially and uniformly rotating models DR and UR, respectively, calculated for the same EOS. Model DR is one of the HMNS models used in BSS [11]. The solutions of Models I, II, III, and UR in Table III are those closest to the maximum mass model of each rotation parameter set. Those of Models IV–V and DR are close to the maximum mass model among the calculated equilibriums. Solution sequences of these models are expected to continue to larger deformations and eventually to completely toroidal configurations. Such toroidal equilibriums may support a much larger mass than the presented solutions. Also note that, in Models II and III, the rotation of the fluid near the equatorial surface is close to the Kepler limit.

In Fig.4, the Arnowitt-Deser-Misner (ADM) mass M_{ADM} is plotted with respect to the maximum of the rest mass density ρ_c . The curves for Models II, III, and UR are the extrapolated maximum values of M_{ADM} for each value of ρ_c . For Models IV, V, and DR which exhibit toroidal configurations, the curves are those of fixed axis ratio $R_z/R_0 = 0.25$, and for Model I, the curve is for $R_z/R_0 = 0.5$. Each solution in Table III is marked by a circle in the plots. It can be seen clearly that hypermassive solutions exist for differential rotation Models I, III–V, and DR, while only supramassive solutions exist for Model II.⁵

⁴ The degree of deformation of an axisymmetric star may be measured by the ratio of the axes along the polar and equatorial radius R_z/R_0 . Each dashed green curve in each panel of Fig.3 corresponds to the shape of a star in the xz plane with a fixed R_z/R_0 . (Each dashed green curve corresponds to the surface of a different solution, and sequences of dashed green curves are deformation sequences of each differentially rotating model.) The contours for ρ and the color map for Ω , as well as the corresponding right panels, are those of the solution with the largest deformation among those computed for each model.

⁵ We call a compact star solution hypermassive if its mass is larger than that of the maximum mass of the uniformly rotating solution, and supramassive if its solution is smaller than the maximum mass of the uniformly rotating solution, but larger than

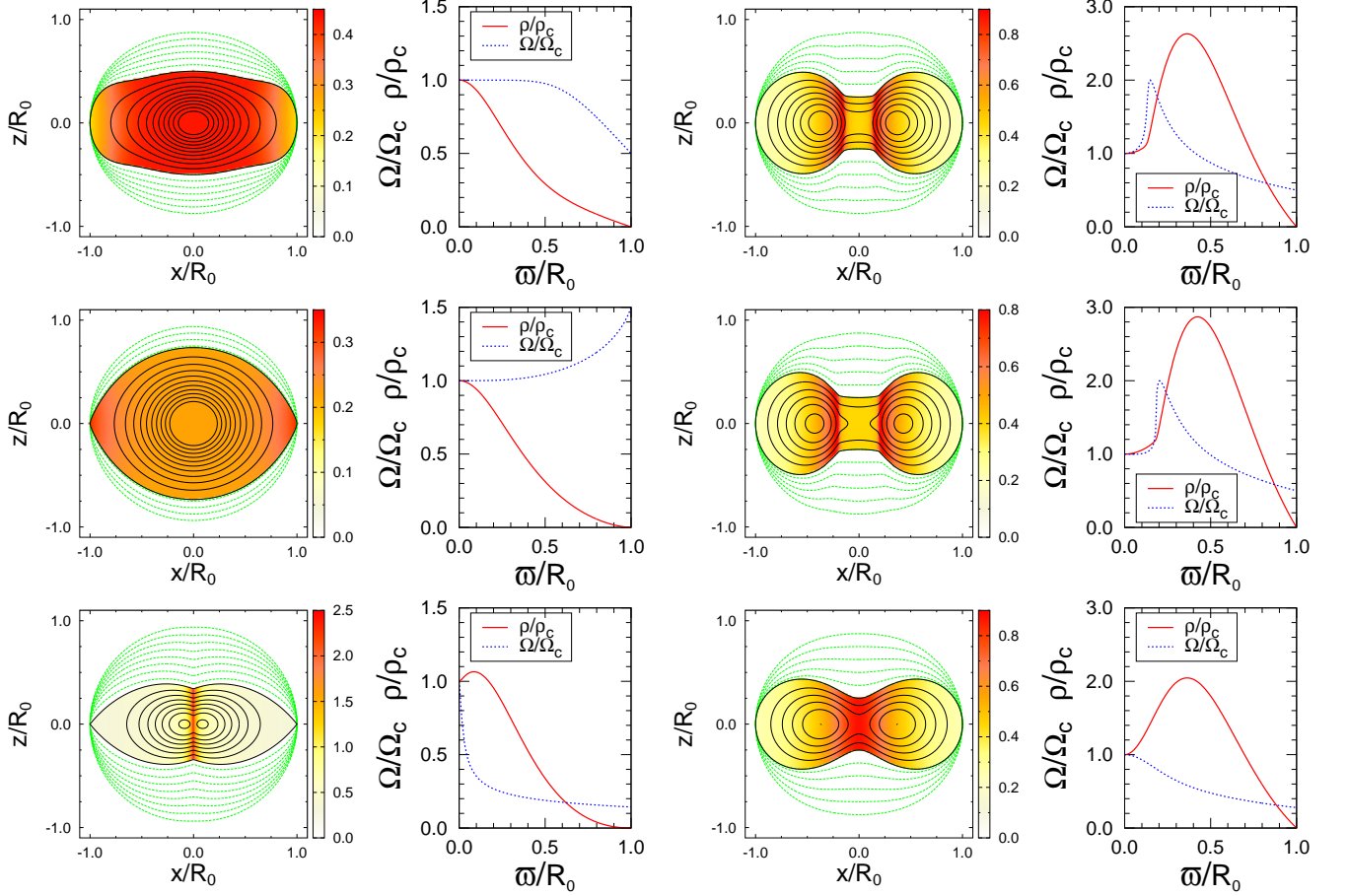


FIG. 3. Equilibria of differentially rotating compact stars. The set of model parameters for the rotation law for each pair of panels is described in Table II. The pairs of panels from top to bottom in the left column, then from top to bottom in the right column correspond to Models I to V and DR in Table II, respectively. The left panel of each pair shows the contours of the rest mass density ρ (black solid curves), the color map for the angular velocity ΩR_0 and the deformation sequence of the surface of the rotating star $R_s(\theta, \phi)$ (green dashed curves) on the xz (meridional) plane. In the right panels, plotted are the normalized rest mass density profiles ρ/ρ_c and the normalized rotation curves Ω/Ω_c along the equatorial axis ($x = \varpi \sin \theta$ with $\theta = \pi/2$).

TABLE III. Selected solutions for various rotation law models. Models I–V and DR correspond to the rotation laws listed in Table II. The uniformly rotating Model UR is also listed for reference. Listed quantities are the equatorial and polar radii in proper length \bar{R}_0 and \bar{R}_z , the maximum density ρ_c , the angular velocity near the rotation axis Ω_c , the ADM mass M_{ADM} , the rest mass M_0 , the proper mass M_{P} , the angular momentum J , the ratio of the kinetic to gravitational energy $T/|W|$, the virial constant I_{vir} , and the Komar mass M_{K} . Details of the definitions are found in [19].

Model	\bar{R}_0	\bar{R}_z/\bar{R}_0	ρ_c [g/cm ³]	Ω_c	M_{ADM}	M_0	M_{P}	J/M_{ADM}^2	$T/ W $	$I_{\text{vir}}/ W $	$ 1 - M_{\text{K}}/M_{\text{ADM}} $
I	12.100	0.54465	2.0178×10^{15}	0.056201	1.90066	2.09398	2.28918	0.79695	0.1623	7.13×10^{-4}	5.14×10^{-5}
II	9.7507	0.76609	2.3309×10^{15}	0.034174	1.48792	1.63360	1.82150	0.43227	0.0494	8.46×10^{-4}	1.59×10^{-5}
III	14.921	0.38561	1.2531×10^{15}	0.226992	1.97116	2.16320	2.31631	0.84818	0.1854	1.06×10^{-3}	4.80×10^{-5}
IV	12.523	0.26763	1.1830×10^{15}	0.062582	2.56462	2.84625	3.07421	0.88534	0.2464	1.60×10^{-4}	2.67×10^{-4}
V	13.501	0.26010	8.6983×10^{14}	0.046783	2.59667	2.86195	3.03360	0.91444	0.2461	8.59×10^{-5}	2.00×10^{-4}
DR	14.230	0.26688	8.6985×10^{14}	0.100879	2.66479	2.94986	3.12656	0.95184	0.2589	1.44×10^{-4}	2.09×10^{-4}
UR	11.141	0.63972	2.3309×10^{15}	0.044776	1.58665	1.74325	1.93925	0.56764	0.0832	8.87×10^{-4}	2.54×10^{-5}

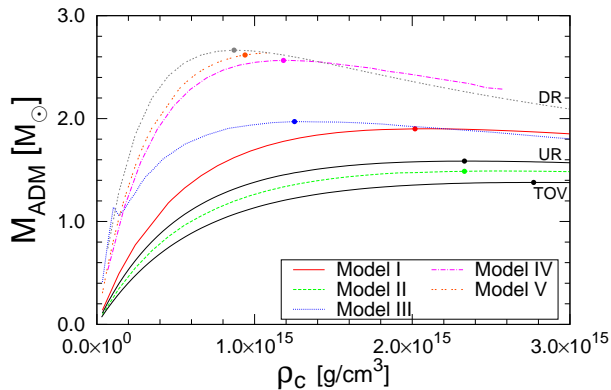


FIG. 4. M_{ADM} is plotted with respect to the maximum rest mass density ρ_c for differentially rotating Models I to V in Table II. For reference, Model DR in Table II [11], the uniformly rotating Model UR and the spherically symmetric (TOV) model are also plotted. The curves for Models II, III and UR correspond to their maximum deformation sequences. Those of Models IV, V, DR correspond to sequences with a fixed axis ratio $R_z/R_0 = 0.25$, and Model I with $R_z/R_0 = 0.5$. Each solution in Table III and the maximum mass of the TOV solution Table I is marked by a circle on each curve.

In Model I (top left column of Fig.3), the differential rotation law is nearly constant in the core, and decreases to 50% of the core value at the equatorial surface. This type of rotation law may be realized in the PNS formed as a result of core collapse. Because of the uniform rotation of the core, the deformation of equilibrium solutions appear to be limited: examining the density contours of several solutions slightly more deformed than that of Model I in Fig.3, we found that, although the surface of the star is not close to the Kepler limit, the largely deformed inner part reaches break-up because of rapid rotation, and hence the deformation sequence of spheroidal equilibria is terminated.

For Model II (the second panel from the top in the left column in Fig.3), the equatorial angular velocity Ω_{eq} of the star is 50% higher than the central value Ω_c . In such a case, the maximum deformation can not be larger than that of the uniformly rotating Model UR. Although Model II is less deformed than Model UR, $\Omega_{\text{eq}} (= 2\Omega_c$ in this case) at the maximally rotating model (Kepler limit) is about 53% *larger* than Ω of the uniformly rotating model (in normalized angular velocity ΩM_{ADM} is 43% larger), while the $T/|W|$ of Model II is 59% *smaller* than that of Model UR. Such solution may become a model for neutron stars spinning up because of equatorial accretion. In more realistic situations, it might be necessary to apply external pressure at the surface of the star, which may allow more rapid rotation than the presented model.

Model III (the third panel from the top of the left column in Fig.3) is an example for which the rotation curve is a power of ϖ . In this model, we choose $q = 4$ in Eq. (5), which becomes $\Omega \sim \varpi^{-2/q} = \varpi^{-0.5}$ in the

Newtonian limit. We have confirmed that this power law is reproduced in the less massive solutions, but in the presented solution which is close to the maximum mass, the index appear to be $\Omega \sim \varpi^{-0.4}$, which is considered to be a relativistic effect in isotropic coordinates.

In the pairs of panels in the right column of Fig.3, equilibrium models largely deformed to become toroidal density distributions are presented. Model IV (top panels) is the result for Eq.(8) with $(p, q) = (1, 3)$, and Model V (middle panels) for Eq.(9) with $p = 3/2$. Model DR (bottom panels) is the model with Eq.(8) with $q = 1$, which is the same as rotation law (1), and is shown for comparison. Model DR has been commonly used for studying HMNS and other relativistic differentially rotating stars including PNS [10–13]. Solution sequences of increasing deformation of these three models seem not to terminate at a certain axis ratio, but continue to toroidal solutions. This allows masses as high as, or even higher than, twice the maximum mass of the spheroidal solution.

Since these differential rotation profiles allow toroidal distributions of mass, these three solutions are qualitatively similar. However, the detailed structure of the solutions, especially near the rotation axis, depends on the rotation curves. The rotation curve is flatter for larger index p , and accordingly, the distance between the rotation axis and the maximum density (center of the toroidal density distribution) becomes wider.

The overall features of the rotation curve of each compact star presented in Fig. 3 are qualitatively the same as the corresponding Newtonian rotation curves shown in Figs. 1 and 2. Differences in the details of the profiles may be due to the use of isotropic coordinates on the spacelike hypersurface, for which the coordinate length becomes relatively short in the region of stronger gravity (with higher density).

IV. DISCUSSION

In recent papers [20, 21], fully numerical relativity simulations for high density matter associated with large shear viscosity have been performed. In [20], the evolution of rotation profiles due to viscosity was shown for the HMNS formed after BNS mergers. Because of the assumption of high viscosity, the rotation profile evolves towards uniform rotation in a short timescale, about ~ 20 msec, and hence the rotating HMNS stably evolves in such short timescale. However, if the viscosity is not strong enough, the evolution timescale of such HMNS may be longer, and then the stability of each rotating model with a certain rotation profile needs to be examined. Our equilibrium models will be useful for studying the stability of such HMNS. As a step for such a study, one can investigate the bar mode instability of differentially rotating neutron stars with the proposed new rotation laws, as it has been done limitedly to rotation law (1) in [22].

We have proposed new function forms of integrabil-

ity conditions for differential rotation laws of relativistic compact stars in equilibrium. It is possible to develop further variations of function forms for other rotation laws. More practically, one could prepare interpolating or fitting functions for a data table of $j(\Omega)$ or $\Omega(j)$ obtained from the results of numerical simulations. In this paper, we have concentrated on the effect of differential rotation on the increase of the maximum mass seen in the HMNS. However, in more realistic situations, the increase of the mass of HMNS is due also to the thermal part of the EOS. It is therefore important to include the thermal part of the EOS to develop more realistic equilibrium models of such PNS or HMNS for distinguishing the contributions from the thermal pressure and the differential rotation to the mass excess. As for GW170817, a search for a rotating neutron star remnant has been

performed in the data following GW170817 and the upper limits of gravitational wave signal is obtained which is of an order of magnitude larger than expected. The signal would be detected by LIGO/VIRGO of the design sensitivity and the such future detectors as KAGRA [23]. Such extensions of the present method and their applications to actual compact objects are the next step of our future works.

ACKNOWLEDGMENTS

This work was supported by JSPS Grant-in-Aid for Scientific Research(C) 15K05085, 17K05447, 26400267, 26400274, NSF Grants PHY-1602536, PHY-1662211, NASA Grants NNX13AH44G, 80NSSC17K0070.

-
- [1] B. P. Abbott *et al.* [LIGO Scientific and Virgo Collaborations], Phys. Rev. Lett. **119**, no. 16, 161101 (2017); Astrophys. J. **848**, L12 (2017)
- [2] For reviews of core collapse and BNS merger simulations, see e.g., H. T. Janka, K. Langanke, A. Marek, G. Martinez-Pinedo and B. Mueller, Phys. Rept. **442**, 38 (2007); H. T. Janka, K. Langanke, A. Marek, G. Martinez-Pinedo and B. Mueller, Phys. Rept. **442**, 38 (2007); M. Shibata, *Numerical Relativity*, World Scientific, Singapore (2016); L. Baiotti and L. Rezzolla, Rept. Prog. Phys. **80**, no. 9, 096901 (2017)
- [3] e.g., C. D. Ott, A. Burrows, T. A. Thompson, E. Livne and R. Walder, Astrophys. J. Suppl. **164**, 130 (2006); A. Burrows, L. Dessart, E. Livne, C. D. Ott and J. Murphy, Astrophys. J. **664**, 416 (2007)
- [4] e.g., K. Hotokezaka, K. Kiuchi, K. Kyutoku, T. Muranushi, Y. i. Sekiguchi, M. Shibata and K. Taniguchi, Phys. Rev. D **88**, 044026 (2013); T. Dietrich, S. Bernuzzi, M. Ujevic and B. Brügmann, Phys. Rev. D **91**, no. 12, 124041 (2015) A. Bauswein and N. Stergioulas, Phys. Rev. D **91**, no. 12, 124056 (2015); W. Kastaun and F. Galeazzi, Phys. Rev. D **91**, no. 6, 064027 (2015); W. Kastaun, R. Ciolfi and B. Giacomazzo, Phys. Rev. D **94**, no. 4, 044060 (2016); W. Kastaun, R. Ciolfi, A. Endrizzi and B. Giacomazzo, arXiv:1612.03671; R. Ciolfi, W. Kastaun, B. Giacomazzo, A. Endrizzi, D. M. Siegel and R. Perna, Phys. Rev. D **95**, no. 6, 063016 (2017); M. Hanauske, K. Takami, L. Bovard, L. Rezzolla, J. A. Font, F. Galeazzi and H. Stöcker, Phys. Rev. D **96**, no. 4, 043004 (2017)
- [5] R. Perna, P. Duffell, M. Cantiello, and A. I. MacFadyen, Astrophys. J., **781**, 119 (2014) T. Nakamura, Prog. Theor. Phys, **70**, 1144 (1983).
- [6] J. L. Friedman and N. Stergioulas, *Rotating Relativistic Stars*, Cambridge University Press, Cambridge, UK, 2013; N. Stergioulas, *Rotating Stars in Relativity*, Living Rev. Relativity **6**, (2003), 3. URL (cited on July 1st 2011): <http://www.livingreviews.org/lrr-2003-3>; R. Meinel, M. Ansorg, A. Kleinwächter, G. Neugebauer, and D. Petroff, *Relativistic Figures of Equilibrium*, Cambridge University Press, New York (2008).
- [7] J. P. Ostriker, and J. W.-K. Mark, Astrophys. J. **151**, 1075 (1968); I. Hachisu, ApJS **62**, 461 (1986)
- [8] E. M. Butterworth, & J. R. Ipser, Astrophys. J., **204**, 200 (1976); Y. Eriguchi, Prog. Theor. Phys., **64**, 2009 (1980); J. L. Friedman, L. Parker and J. R. Ipser, Astrophys. J. **304**, 115 (1986); H. Komatsu, Y. Eriguchi and I. Hachisu, Mon. Not. Roy. Astron. Soc. **237**, 355 (1989). N. Stergioulas and J. L. Friedman, Astrophys. J. **444**, 306 (1995); S. Bonazzola, E. Gourgoulhon and J. A. Marck, Phys. Rev. D **58**, 104020 (1998); M. Ansorg, A. Kleinwächter and R. Meinel, Astron. Astrophys. **405**, 711 (2003); G. B. Cook, S. L. Shapiro and S. A. Teukolsky, Astrophys. J. **422**, 227 (1994);
- [9] J.-L. Tassoul, *Theory of Rotating Star*, Princeton Series in Astrophysics, Princeton University Press, 1978,
- [10] H. Komatsu, Y. Eriguchi, and I. Hachisu, Mon. Not. Roy. Astron. Soc. **239**, 153 (1989); M. Ansorg, D. Gondek-Rosinska, L. Villain and M. Bejger, EAS Publ. Ser. **30**, 373 (2008); D. Gondek-Rosinska, I. Kowalska, L. Villain, M. Ansorg and M. Kucaba, Astrophys. J. **837**, no. 1, 58 (2017); A. M. Studzinska, M. Kucaba, D. Gondek-Rosinska, L. Villain and M. Ansorg, Mon. Not. Roy. Astron. Soc. **463**, no. 3, 2667 (2016);
- [11] T. W. Baumgarte, S. L. Shapiro and M. Shibata, Astrophys. J. **528**, L29 (2000)
- [12] I. A. Morrison, T. W. Baumgarte and S. L. Shapiro, Astrophys. J. **610**, 941 (2004);
- [13] J. D. Kaplan, C. D. Ott, E. P. O'Connor, K. Kiuchi, L. Roberts and M. Duez, Astrophys. J. **790**, 19 (2014)
- [14] F. Galeazzi, S. Yoshida and Y. Eriguchi, Astron. Astrophys. **541**, A156 (2012)
- [15] A. Bauswein and N. Stergioulas, Mon. Not. Roy. Astron. Soc. **471**, 4956 (2017); G. Bozzola, N. Stergioulas and A. Bauswein, arXiv:1709.02787 [gr-qc].
- [16] K. Uryu, A. Tsokaros, F. Galeazzi, H. Hotta, M. Sugimura, K. Taniguchi and S. Yoshida, Phys. Rev. D **93**, no. 4, 044056 (2016).
- [17] P. Mach and E. Malec, Phys. Rev. D **91**, no. 12, 124053 (2015); J. Karkowski, P. Mach, E. Malec, M. Pirog and N. Xie, Phys. Rev. D **94**, no. 12, 124041 (2016)
- [18] M. A. Abramowicz, Acta Astronomica **21**, 81 (1971)

- [19] X. Huang, C. Markakis, N. Sugiyama and K. Uryu, Phys. Rev. D **78**, 124023 (2008); K. Uryu and A. Tsokaros, Phys. Rev. D **85**, 064014 (2012); K. Uryu, A. Tsokaros and P. Grandclement, Phys. Rev. D **86**, 104001 (2012); K. Uryu, A. Tsokaros, L. Baiotti, F. Galeazzi, N. Sugiyama, K. Taniguchi and S. Yoshida, Phys. Rev. D **94**, no. 10, 101302 (2016)
- [20] M. Shibata, K. Kiuchi and Y. I. Sekiguchi, Phys. Rev. D **95**, no. 8, 083005 (2017); M. Shibata and K. Kiuchi, Phys. Rev. D **95**, no. 12, 123003 (2017)
- [21] D. Radice, Astrophys. J. **838**, no. 1, L2 (2017)
- [22] M. Shibata, T. W. Baumgarte and S. L. Shapiro, Astrophys. J. **542**, 453 (2000); M. Saijo, M. Shibata, T. W. Baumgarte and S. L. Shapiro, Astrophys. J. **548**, 919 (2001); M. Shibata, S. Karino and Y. Eriguchi, Mon. Not. Roy. Astron. Soc. **343**, 619 (2003); L. Baiotti, R. De Pietri, G. M. Manca and L. Rezzolla, Phys. Rev. D **75**, 044023 (2007); G. M. Manca, L. Baiotti, R. De Pietri and L. Rezzolla, Class. Quant. Grav. **24**, S171 (2007); N. Stergioulas, A. Bauswein, K. Zagkouris and H. T. Janka, Mon. Not. Roy. Astron. Soc. **418** (2011) 427; R. De Pietri, A. Feo, L. Franci and F. Löffler, Phys. Rev. D **90**, no. 2, 024034 (2014); F. Löffler, R. De Pietri, A. Feo, F. Maione and L. Franci, Phys. Rev. D **91**, 064057 (2015)
- [23] B. P. Abbott *et al.* [LIGO Scientific and Virgo Collaborations], arXiv:1710.09320 [astro-ph.HE].